Neutrino-induced neutral- and charged-current reactions on ^{40}Ar

Toshio Suzuki[1,2,3,*] and Noritaka Shimizu[4]

[1]*Department of Physics, College of Humanities and Sciences, Nihon University Sakurajosui 3-25-40, Setagaya-ku, Tokyo 156-8550, Japan*
[2]*NAT Research Center, NAT Corporation, 3129-45 Hibara Muramatsu, Tokai-mura, Naka-gun, Ibaraki 319-1112, Japan*
[3]*School of Physics, Beihang University, 37 Xueyuan Road, Haidian-qu, Beijing 100083, People's Republic of China*
[4]*Center for Computational Sciences, University of Tsukuba, 1-1-1 Tennodai, Tsukuba, Ibaraki 305-8577, Japan*

(Received 12 April 2023; accepted 12 July 2023; published 21 July 2023)

Neutrino-induced reactions on ^{40}Ar are investigated by the shell model for Gamow-Teller transitions and the random-phase approximation (RPA) for forbidden transitions. For the 1^+ multipole, an effective interaction in the *sd-pf* shell obtained by the extended Kuo-Krenciglowa (EKK) method from chiral interactions is used to study $B(\mathrm{GT})$, the charged-current reaction $^{40}\mathrm{Ar}(\nu_e, e^-)^{40}\mathrm{K}$, $B(M1)$ in ^{40}Ar, and the neutral-current reaction $^{40}\mathrm{Ar}(\nu, \nu')^{40}\mathrm{Ar}$. A considerable quenching for spin modes is found in the analysis of $B(M1)$, and this quenching is taken into account for the evaluation of the cross sections of the neutral-current reaction. The sensitive dependence of the reaction cross sections on the quenching of the axial-vector coupling constant, g_A, is pointed out.

DOI: 10.1103/PhysRevC.108.014611

I. INTRODUCTION

The study of low-energy neutrinos and neutrino-nucleus interactions is important for unveiling the properties of neutrinos such as mass hierarchy and *CP*-violating phase, which are still open problems, as well as physics beyond the standard model such as neutrino magnetic moment, nonstandard interactions, and sterile neutrinos [1]. Detection of supernova neutrinos is crucial to study supernova dynamics, neutrino oscillations in matter, and nucleosynthesis [2]. Liquid Ar detectors such as liquid argon time projection chambers (LATPCs) [3] are important tools for the study of neutrino properties by detection of supernova and decay-at-rest (DAR) neutrinos. The DAR neutrinos are now available at the Spallation Neutron Source at Oak Ridge National Laboratory (ORNL) [4]. Detection of supernova neutrinos is planned at Super-Kamiokande [5], Hyper-Kamiokande [6], the Deep Underground Neutrino Experiment (DUNE) [7], and the Jiangmen Underground Neutrino Observatory (JUNO) [8].

Here, neutrino-induced reactions on ^{40}Ar are studied for neutrino energies at $E_\nu \leqslant 100$ MeV by a hybrid model [9,10], where Gamow-Teller (GT) transitions are treated by the shell model while the random-phase approximation (RPA) is employed for forbidden transitions. The multipole expansion method of Walecka [11] is used for the evaluations of neutrino-induced reaction cross sections. The GT part of the charged-current reaction $^{40}\mathrm{Ar}(\nu_e, e^-)^{40}\mathrm{K}$ was investigated with the use of a shell-model Hamiltonian for the *sd-pf* shell [10], where the *sd-pf* cross-shell is taken to be the monopole-based universal interaction (VMU) [12]. The VMU consists of tensor components of $\pi + \rho$ meson exchanges and central components with one-range Gaussian form. The monopole terms of the tensor interaction have a general sign rule: attractive for $j_> = \ell + 1/2$ and $j_< = \ell - 1/2$ orbits and repulsive for $j_>$-$j_>$ and $j_<$-$j_<$ orbits [13]. Monopole terms of microscopic *G* matrix and good phenomenological interactions such as SDPF-M [14] and GXPF1A [15] have characteristic orbit dependences, that is, a kinked structure consistent with this general rule, and this feature can be attributed to the tensor components of the interactions [12]. The important roles of the tensor interaction are thus universal in effective interactions, and the use of the VMU for the cross-shell part is based on the general features of the monopole terms of the tensor interaction shown above.

The experimental GT strength obtained by (p, n) reactions [16] was found to be well reproduced by these shell-model studies [10]. Shell-model calculations can take into account more correlation effects compared to the RPA methods, while the cross sections were also obtained by quasiparticle RPA (QRPA) [17] and continuum RPA (CRPA) calculations [18]. Here, we use another shell-model Hamiltonian for the *sd-pf* shell recently obtained by the extended Kuo-Krenciglowa (EKK) method [19,20] from the low-momentum interaction $V_{\mathrm{low}k}$, derived from chiral effective interactions. The chiral N^{3}LO interaction of Entem and Machleid [21] is renormalized by the $V_{\mathrm{low}k}$ approach [22,23] with a cutoff at $\Lambda = 2.0$ fm^{-1}. The effective shell-model interaction in the model space (*P* space) is derived starting from the renormalized $V_{\mathrm{low}k}$ by many-body perturbation theory (MBPT) based on the so-called *Q*-box technique with folded-diagram expansion [24–27]. As the conventional MBPTs—the Kuo-Krenciglowa (KK) method [25,28] and the Lee-Suzuki method [29]—are constructed for degenerate model space, these methods cannot be used for nondegenerate *sd-pf* shell model space. These approaches have been

---

[*] suzuki.toshio@nihon-u.ac.jp

generalized to nondegenerate model spaces in terms of multienergy Q boxes. [30]. Though a distinct improvement was noticed for the multienergy Q-box method in schematic models, these models have not been applied to practical calculations.

The VMU, therefore, is often used for the cross-shell part of the interaction and proves to be successful in many cases, for example in SDPF-MU [31] for the sd-pf shell, YSOX [32] for the p-sd shell, and effective interactions in the Pb region [33]. The sd-pf cross-shell part of the effective interaction used for ^{40}Ar, referred to as SDPF-VMU-LS [10], includes also the two-body spin-orbit interaction from meson-exchanges, and sd- and pf-shell parts are those of phenomenological SDPF-M [14] and GXPF1A [15] interactions, respectively.

Here, we use the extended KK (EKK) method proposed by Takayanagi [34], where one energy parameter is introduced to avoid the divergence problem in the Q-box expansion that arises for nondegenerate model spaces in the conventional KK method [19]. Recently, the effective shell-model Hamiltonian for the nondegenerate sd-pf shell was obtained by the EKK method starting from $V_{\text{low}k}$, derived from the chiral N^{3}LO interaction [21], including up to third-order Q-box expansions [20]. The effective interaction with the additional Fujita-Miyazawa three-nucleon (3N) interaction [35], referred to as EEdf1 [36], is found to explain the energy spectra, electric quadrupole (E2) transition strengths, and drip lines of the F, Ne, Na, and Mg isotopes quite well [20,37].

The GT strength and cross sections for ^{40}Ar$(\nu_e, e^-)^{40}$K evaluated by the new effective interaction with the EKK method are discussed in Sec. II. The effective axial-vector coupling constant g_A^{eff}, which can reproduce the experimental GT strength, is used to obtain the charged-current reaction cross section for the 1$^+$ multipole. In Sec. III, magnetic dipole (M1) transition strength and neutral-current reaction cross sections for ^{40}Ar are evaluated by the effective interaction obtained by the EKK method for the 1$^+$ multipole and by RPA for forbidden transitions. The quenching of the spin-dependent transition strength is determined to reproduce the experimental M1 data, and the neutral-current reaction cross sections are obtained with the inclusion of the quenching effects for the 1$^+$ multipole. Sensitivity of the neutral-current reaction cross sections to the quenching of the axial-vector coupling constant g_A is discussed. The summary is given in Sec. IV.

II. CHARGED-CURRENT REACTIONS

We discuss GT strength in ^{40}Ar and the charged-current reaction ^{40}Ar$(\nu_e, \mathrm{e}^-)^{40}$K. A modified version of the shell-model Hamiltonian, EEdf1 [20,36], obtained by the EKK method in the sd-pf shell is employed. In the present work, we use the effective interaction with the chiral N^{2}LO 3N interaction [38] instead of the Fujita-Miyazawa 3N force. The density-dependent nucleon-nucleon (NN) interaction is first derived from the 3N interaction by folding over the third nucleon in the Fermi sea [39], and then the effective NN interaction is obtained by having the density dependence integrated out with the normal density [37]. The new interaction, which will be referred to as EEdf2S hereafter, can also explain the spectroscopic properties of the neutron-rich isotopes as well.

The GT strength in ^{40}Ar is evaluated by shell-model calculations with the use of EEdf2S in $sd^{-2}pf^2 + sd^{-4}pf^4$ configurations using the KSHELL code [40]. As the shell-model calculations are done in two major shells, a center-of-mass (c.m.) correction is needed to remove the spurious components which come from the c.m. motion. The method by Gloeckner and Lawson [41] is used for the c.m. correction. In the calculations, the c.m. Hamiltonian $H_{\text{c.m.}}$ is added to the original shell-model Hamiltonian H_{SM}: $H' = H_{\text{SM}} + \beta H_{\text{c.m.}}$. The value of β is taken large enough so that the effects of the c.m. motion become negligible in low-lying states. Here, we adopt $\frac{\beta\hbar\omega}{A} = 30$ MeV for the EEdf2S interaction and $\frac{\beta\hbar\omega}{A} = 10$ MeV for the SDPF-VMU-LS interaction (see Ref. [14] also).

The quenching factor for the axial-vector coupling constant, $q_A = g_A^{\text{eff}}/g_A$, is determined to be consistent with the experimental GT strength, and it is obtained to be $q_A = 1$. When the phenomenological SDPF-VMU-LS interaction was used for the sd-pf cross-shell part, the configuration space was limited to $sd^{-2}pf^2$ and $q_A = 0.775$ was adopted [10]. The calculated results for the cumulative sum of B(GT) obtained for EEdf2S and SDPF-VMU-LS as well as the experimental data [16] are shown in Fig. 1(a). B(GT) is defined by

$$B(GT) = \frac{1}{2J_i + 1}\left|\langle f||q_A \sum_i \vec{\sigma}_i t_{-,i}||i\rangle\right|^2, \tag{1}$$

where J_i is the spin of the initial state and $t_-|n\rangle = |p\rangle$, and the sum over nucleons i is taken. Both the EEdf2S with $q_A = 1$ and the SDPF-VMU-LS with $q_A = 0.775$ explain rather well the B(GT) strengths in ^{40}Ar, though the strength is lower in the low excitation energy region and higher in the high excitation energy region for EEdf2S. The charged-current reaction cross sections for ^{40}Ar$(\nu_e, e^-)^{40}$K for the excitations of the 1$^+$ states are obtained with the use of q_A determined from the analysis of the GT strength. The cross sections for the sum of the 1$^+$ and 0$^+$ multipoles are compared in Fig. 1(b). The cross sections obtained by the two interactions are found to be close to each other. The difference between them is as small as within 5%. The cross sections for ^{40}Ar$(\nu_e, e^-)^{40}$K obtained by the hybrid model in Ref. [10] thus remain almost unchanged when the EEdf2S interaction is used for the GT part.

III. NEUTRAL-CURRENT REACTIONS

A. Magnetic dipole strength in ^{40}Ar

Now we discuss neutral-current reactions on ^{40}Ar. Experimental information on the magnetic dipole (M1) strength in ^{40}Ar is available [42]. The M1 strength was measured by linearly polarized monochromatic γ scatterings on ^{40}Ar in the range of excitation energies E_x = 7.7–11 MeV. One peak of the strength was found at E_x = 9.757 MeV with $B(M1) = 0.149 \pm 0.059\, \mu_N^2$ [42]. $B(M1)$ is defined as

$$B(M1) = \frac{1}{2J_i + 1}\left|\langle f||\sqrt{\frac{3}{4\pi}}(g_s\vec{s}_i + g_\ell\vec{\ell}_i)\mu_N||i\rangle\right|^2, \tag{2}$$

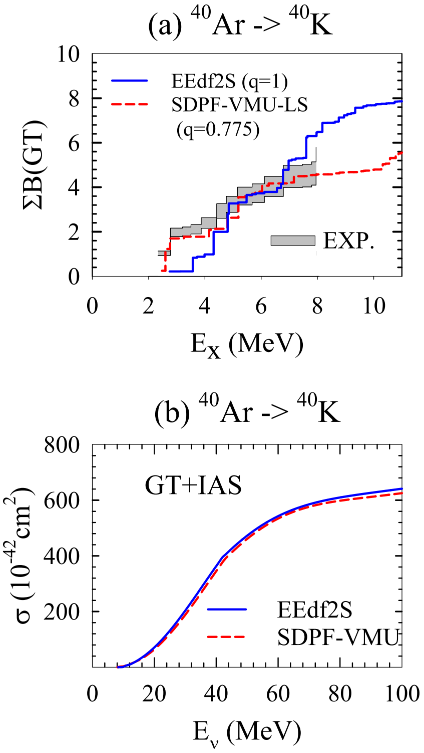

FIG. 1. (a) Cumulative sum of the GT strength for ^{40}Ar → ^{40}K up to excitation energies of ^{40}K, E_x, obtained by the shell-model calculation with the use of EEdf2S and SDPF-VMU-LS [10] interactions. The experimental data [16] are shown by the shaded area. (b) Calculated reaction cross sections for ${}^{40}\mathrm{Ar}(\nu_e, e^-){}^{40}\mathrm{K}$. Contributions from the GT and isobaric analog (IA) transitions obtained by the shell-model calculations with the use of EEdf2S and SDPF-VMU-LS are shown.

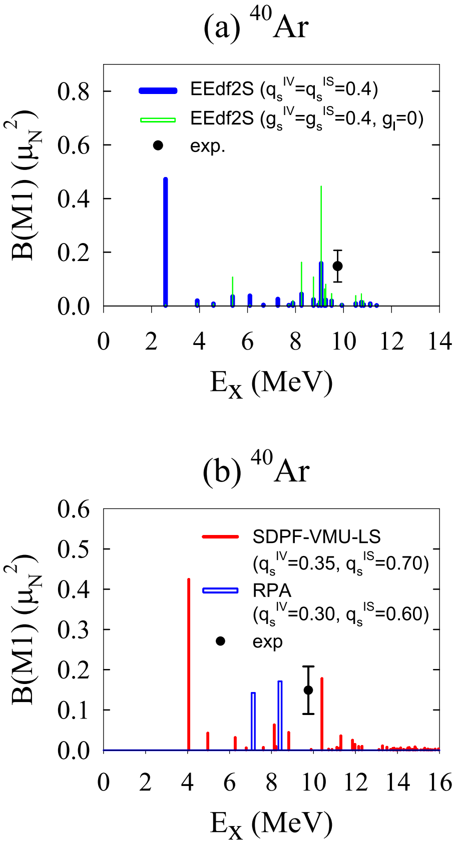

FIG. 2. (a) Calculated $B(M1)$ values in ^{40}Ar obtained by shell-model calculations with the EEdf2S interaction. The quenching factors for the spin g factors are taken to be $q_s^{\mathrm{IV}} = q_s^{\mathrm{IS}} = 0.4$. Thin hollow histograms are obtained with $g_\ell = 0$. Experimental data [42] are also denoted. (b) The same as in (a) for the shell-model calculations with the SDPF-VMU-LS [10] interaction with the quenching factors $q_s^{\mathrm{IV}} = 0.35$ and $q_s^{\mathrm{IS}} = 0.70$ (red filled histograms), and for RPA calculations with SGII [46] with the quenching factors $q_s^{\mathrm{IV}} = 0.30$ and $q_s^{\mathrm{IS}} = 0.60$ (blue hollow histograms).

where g_s and g_ℓ are spin and orbital g factors, respectively, and μ_N is the nucleon magneton. The quenching of the g factors is taken into account. The isovector (isoscalar) quenching factor for g_s is defined by $q_s^{\mathrm{IV}} = g_s^{\mathrm{IV,eff}}/g_s^{\mathrm{IV}}$ ($q_s^{\mathrm{IS}} = g_s^{\mathrm{IS,eff}}/g_s^{\mathrm{IS}}$) with $g_s^{\mathrm{IV}} = -4.70$ ($g_s^{\mathrm{IS}} = 0.88$). The isovector orbital g factor is modified by $\delta g_\ell^{\mathrm{IV}} = -(0.10\text{–}0.15)$ due to meson-exchange current contributions [43,44]. Here, g_ℓ is taken to be $g_\ell = 1.15$ for protons and $g_\ell = -0.15$ for neutrons. The quenching of the spin g factors depends on the interaction and configuration space. Here, they are determined to reproduce the experimental $B(M1)$ data. The quenching of the spin mode thus obtained is used to evaluate the neutral-current reaction cross sections on ^{40}Ar.

$B(M1)$ is evaluated by shell-model calculations with the use of the EEdf2S with $sd^{-2}pf^2 + sd^{-4}pf^4$ configurations. Calculated results for the quenching $q_s^{\mathrm{IV}} = q_s^{\mathrm{IS}} = 0.4$ are shown in Fig. 2(a). The peaks shown in the figure are for the transitions to the 1^+ states with isospin $T = 2$. Note that the main transitions to $T = 1$ states in the charged-current case are missing for the neutral-current channel. The quenching of spin modes in the transitions for $T = 2 \rightarrow T = 2$ could be different from those for $T = 2 \rightarrow T = 1$. Higher isospin states generally need more configurations to construct the eigenstates of the isospin [45]. The experimental $B(M1)$ strength at $E_x = 9.757$ MeV is found to be well reproduced with the EEdf2S although the peak energy is shifted towards the lower energy region by 0.69 MeV. The dominant contributions come from the proton $d_{5/2} \rightarrow d_{3/2}$ transition. When considering the experimental error bar for $B(M1)$, the quenching factor is obtained to be $q_s^{\mathrm{IV}} = 0.39 \pm 0.04$ if $q_s^{\mathrm{IS}} = q_s^{\mathrm{IV}}$ is assumed. It is not possible to get a unique q_s from one observed $B(M1)$ value. Setting different values for q_s^{IV} and q_s^{IS}, for example $q_s^{\mathrm{IS}} = 2q_s^{\mathrm{IV}}$, the experimental $B(M1)$ value is also well reproduced for $q_s^{\mathrm{IV}} = 0.35 \pm 0.04$. The calculated $B(M1)$ for the case of $g_\ell = 0$ are shown by thin hollow histograms in Fig. 2(a). The disappearance of the peak at $E_x = 2.58$ MeV denotes that the 1^+ state has no spin components and the M1 mode is a pure orbital motion.

Calculated $B(M1)$ obtained for the SDPF-VMU-LS interaction used in Ref. [10] for the $sd^{-2}pf^2$ configurations are shown in Fig. 2(b). The quenching factors $q_s^{\mathrm{IV}} = 0.35$ and $q_s^{\mathrm{IS}} = 0.70$ and the same g_ℓ as for EEdf2S are used. The experimental $B(M1)$ is rather well explained, although the peak is at $E_x = 10.40$ MeV, which is 0.64 MeV above the experimental energy. For $q_s^{\mathrm{IV}} = q_s^{\mathrm{IS}} = 0.35$, there appear

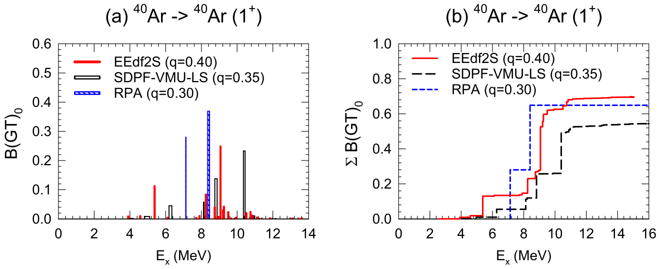

FIG. 3. (a) Red filled, black hollow, and blue shaded histograms denote calculated $B(\mathrm{GT})_0$ values in ^{40}Ar obtained by shell-model calculations with EEdf2S and SDPF-VMU-LS as well as by RPA calculations with SGII with the quenching factors for g_A, $q_A = 0.40$, 0.35, and 0.30, respectively. (b) The same as in (a) for the cumulative sum of the $B(\mathrm{GT})_0$ up to excitation energies E_x.

two $M1$ peaks with similar strength at $E_x = 8.82$ and 10.40 MeV. The former peak has dominant contributions from the neutron $f_{7/2} \rightarrow f_{5/2}$ transition. This suggests that a higher q_s^{IS} value is favored for SDPF-VMU-LS.

The $B(M1)$ values are also evaluated by RPA. A simple configuration, $\pi d_{3/2}^{-2}\, \nu f_{7/2}^{2}$, outside the ^{40}Ca core is assumed for the ground state. The calculated $B(M1)$ obtained with the SGII interaction [46] is shown in Fig. 2(b) for $q_s^{\mathrm{IV}} = 0.30$ and $q_s^{\mathrm{IS}} = 0.60$. Two peaks are obtained at $E_x = 7.13$ and 8.40 MeV. Dominant contributions come from proton $d_{5/2} \rightarrow d_{3/2}$ and neutron $f_{7/2} \rightarrow f_{5/2}$ transitions for the states at 7.13 and 8.40 MeV, respectively. When $q_s^{\mathrm{IV}} = q_s^{\mathrm{IS}} = 0.30$ is adopted, the first peak with proton components disappears and the second peak with neutron components remains with enhanced strength. The pure orbital $M1$ mode is not seen as it is shifted below the ground state in the present calculation. The agreement of the calculated $B(M1)$ with the experiment is not so good as that of the shell-model calculations.

B. Gamow-Teller strength and reaction cross sections for 1$^+$

In this subsection, we discuss GT transitions in the neutral-current channel and reaction cross sections for the 1$^+$ multipole. The GT transition strength, $B(\mathrm{GT})_0$, in the non-charge-exchange channel is defined by

$$B(\mathrm{GT})_0 = \frac{1}{2J_i + 1} \left| \langle f || q_A \sum_i \vec{\sigma}_i \tau_z^i || i \rangle \right|^2. \tag{3}$$

Calculated $B(\mathrm{GT})_0$ obtained by shell-model calculations with EEdf2S and SDPF-VMU-LS as well as RPA calculations are shown in Fig. 3(a). The quenching factor for g_A is taken to be the same as g_s^{IV} obtained in Sec. III A, that is, $q_A = 0.40$, 0.35 for EEdf2S and SDPF-VMU-LS, respectively, and $q_A = 0.30$ for RPA with the SGII. The strength is most spread for EEdf2S, with the largest configuration space among the three cases. The cumulative sums of $B(\mathrm{GT})_0$ are also shown in Fig. 3(b). The total strength is the largest for EEdf2S.

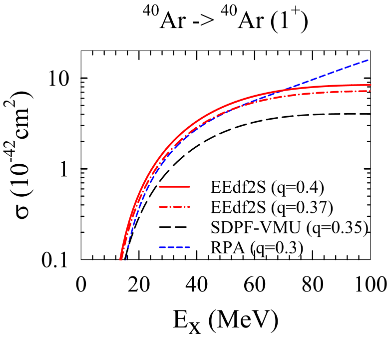

FIG. 4. Calculated cross sections for $^{40}\mathrm{Ar}(\nu, \nu')\,^{40}\mathrm{Ar}$ for the 1$^+$ multipole, obtained by shell-model calculations with EEdf2S for $q_A = 0.4$ and 0.37 and SDPF-VMU-LS for $q_A = 0.35$. Results for RPA calculations with $q_A = 0.3$ are also shown.

Cross sections for the 1$^+$ multipole are evaluated for the shell model and RPA. The energy of the strength is shifted so that the main peak of $B(\mathrm{GT})_0$ with the dominant proton d orbit components becomes equal to the experimental energy, $E_x = 9.757$ MeV. The calculated results are shown in Fig. 4 for EEdf2S with $q_A = 0.40$ and 0.37, SDPF-VMU-LS with $q_A = 0.35$, and RPA with $q_A = 0.30$. The cross section for RPA is close to that for EEdf2S with $q_A = 0.37$, though the GT strength distributions are different: there is little spreading of the strength for the RPA case.

C. Neutral-current reaction cross sections

As the neutrino energy increases, contributions from spin-dipole transitions become important in addition to the GT transitions. The contributions of multipoles except for 1$^+$ are evaluated by RPA calculations. The sum of the spin-dipole strength, $S^{\lambda}(\mathrm{SD})$, energy-weighted sum of the strength, EWS$^{\lambda}$, and averaged energy, $\bar{E}^{\lambda}$, are defined as [47]

$$S^{\lambda}(\mathrm{SD}) = \sum_{i,\mu} \left| \langle \lambda\mu, i | S_{\mu}^{\lambda} | 0 \rangle \right|^2,$$

$$\mathrm{EWS}^{\lambda} = \sum_{i,\mu} (E_i - E_0) \left| \langle i | S_{\mu}^{\lambda} | 0 \rangle \right|^2 = \langle 0 | [S^{\lambda^{\dagger}}, [H, S^{\lambda}]] | 0 \rangle,$$

$$\bar{E}^{\lambda} = EWS^{\lambda} / S^{\lambda}(SD) \tag{4}$$

for the spin-dipole operator

$$S_{\mu}^{\lambda} = [rY^1(\hat{r}) \times \vec{\sigma}]_{\mu}^{\lambda} \tau_z. \tag{5}$$

The energy-weighted sums for the kinetic energy $K = \sum_i \frac{p_i^2}{2m}$ with m the nucleon mass, and one-body spin-orbit potential, $V_{\mathrm{LS}} = -\xi \sum_i \vec{\ell}_i \cdot \vec{\sigma}_i$, are given as [47,48]

$$\mathrm{EWS}_K^{\lambda} = \frac{3}{4\pi} h_{\lambda} \frac{\hbar^2}{2m} A \left[1 + \frac{f_{\lambda}}{3A} \langle 0 | \sum_i \vec{\ell}_i \cdot \vec{\sigma}_i | 0 \rangle \right],$$

$$\mathrm{EWS}_{\mathrm{LS}}^{\lambda} = \frac{3}{4\pi} h_{\lambda} \frac{f_{\lambda}}{3} \xi \langle 0 | \sum_i \left(r_i^2 + g_{\lambda} r_i^2 \vec{\ell}_i \cdot \vec{\sigma}_i \right) | 0 \rangle, \tag{6}$$

where $h_{\lambda} = 2\lambda + 1$, $f_{\lambda} = 2$, 1, and -1 for $\lambda^{\pi} = 0^-$, 1^-, and 2^-, respectively, and $g_{\lambda} = 1$ for $\lambda^{\pi} = 0^-$, 1^- and $g_{\lambda} = -7/5$ for $\lambda^{\pi} = 2^-$.

For ^{40}Ar, as the term $\langle 0 | \sum_i \vec{\sigma}_i \cdot \vec{\ell}_i | 0 \rangle$ does not vanish and has positive value for the $d_{3/2}^{-2} f_{7/2}^{2}$ configuration, $\mathrm{EWS}_K^{\lambda}/(2\lambda + 1)$ decreases as the value of λ increases. Note

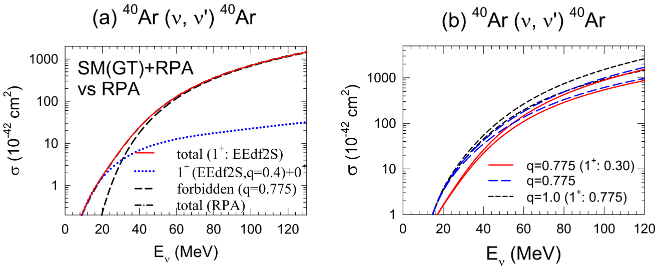

FIG. 5. (a) Calculated neutral-current reaction cross sections obtained by the hybrid model. The contributions from the 1^+ multipole are evaluated by the shell model with EEdf2S, while forbidden transitions are obtained by RPA. The total cross sections, cross sections for 1^+ and 0^+ multipoles, and those for the forbidden transitions are denoted by solid, dotted, and dashed curves, respectively. Cross sections evaluated by RPA for all the multipoles are shown by the dash-dotted curve. (b) Dependence of the total cross sections obtained by RPA on the quenching factor of g_A. Calculated cross sections with $q_A = 0.30$ for 1^+ and q_A =0.775 for other multipoles are shown by solid curves. Those with $q_A = 0.775$ for all the multipoles are shown by long-dashed curves, while short-dashed curves denote those with $q_A = 0.775$ for 1^+ and $q_A = 1.0$ for other multipoles. Larger cross sections denote those for (ν, ν') reactions, while smaller ones are for $(\bar{\nu}, \bar{\nu}')$ reactions.

that $\mathrm{EWS}_{\mathrm{LS}}^{\lambda=2}$ is also reduced by the spin-orbit potential. As the sum of the strength is roughly proportional to $2\lambda + 1$, the averaged energy is expected to follow the order $\bar{E}^2 < \bar{E}^1 < \bar{E}^0$. For the Hamiltonian of the sum of kinetic energy and one-body spin-orbit potential, $S^\lambda(\mathrm{SD}) = 12.53$, 36.36, and 56.47 fm^2, $\mathrm{EWS}_{K+LS}^\lambda = 333.2$, 796.7, and 814.1 MeV fm^2, and $\bar{E}^\lambda = 26.58$, 21.92, and 14.42 MeV for 0^-, 1^-, and 2^-, respectively. The order of the averaged energies is $\bar{E}^2 < \bar{E}^1 < \bar{E}^0$ as expected. The kinetic energy and one-body spin-orbit interaction in the Hamiltonian lead to the splitting of the spin-dipole strength. Two-body spin-dependent interactions further affect the distribution of the strength. When spin-dependent interactions in SGII are added, $S^\lambda(\mathrm{SD})$ become 14.87, 57.02, and 52.04 fm^2, EWS^λ are enhanced to 369.6, 1241.0, and 817.4 MeV fm^2, and $\bar{E}^\lambda$ are found to be 24.85, 21.76, and 15.71 MeV for 0^-, 1^-, and 2^-, respectively. The sum of the strength and the EWS for 1^- are found to be greatly enhanced by the spin-dependent interactions, while the order of $\bar{E}^\lambda$ remains the same.

Reaction cross sections for ^{40}Ar (ν, ν') ^{40}Ar for multipoles other than 1^+ are obtained by RPA calculations with SGII including up to $J^\pi = 4^\pm$. The quenching for g_A is taken to be $q_A = 0.775$ [10]. Calculated cross sections for 0^+ and 1^+ multipoles, for forbidden transitions, as well as for the total contributions are shown in Fig. 5(a). The 1^+ multipole part is obtained by the shell model with the EEdf2S with the quenching factor $q_A = 0.40$. Contributions from forbidden transitions become important at $E_\nu > 30$ MeV. As the sum of the strength is largest for 1^-, the contributions from the 1^- multipole become most important at $E_\nu > 40$ MeV, while those from the 2^- multipole are more important at $E_\nu < 40$ MeV due to its lower averaged energy compared with 1^-. We notice that, when the 1^+ multipole part is evaluated by RPA with $q_A = 0.30$ instead of the shell model, the total cross section remains almost unchanged. In the present work, the quenching factor for g_A in the 1^+ multipole is constrained by the experimental $B(M1)$ data.

Calculated cross sections are sensitive to the choice of the quenching factor for g_A. Dependence of the total cross sections obtained by RPA calculations on the quenching factor of g_A is shown in Fig. 5(b) for both neutrino and antineutrino scatterings. When the quenching for the 1^+ multipole is taken to be the same as in the charged-current reaction, that is, $q_A = 0.775$ instead of $q_A = 0.30$, the cross sections are enhanced more than twice at $E_\nu < 40$ MeV. When $q_A = 1$ is adopted instead of $q_A = 0.775$ for the forbidden transitions, as is usually done in many RPA calculations, the cross sections are enhanced also at higher E_ν and become close to those in Refs. [18,49]. It is, thus, important to determine q_A carefully.

IV. SUMMARY

ν-induced neutral- and charged-current reaction cross sections on ^{40}Ar are studied by a hybrid model, where the GT transitions and forbidden transitions are treated by the shell model and RPA, respectively. An effective interaction in the *sd*-*pf* shell constructed by the EKK method [20,37], referred to as EEdf2S, is used to evaluate $B(\mathrm{GT})$, $B(M1)$, and reaction cross sections for the 1^+ multipole with a wide configuration space, $sd^{-2}pf^2 + sd^{-4}pf^4$. Calculated $B(\mathrm{GT})$ in ^{40}Ar reproduces rather well the experimental data with $q_A = g_A^{\mathrm{eff}}/g_A = 1$. The calculated cross sections for $^{40}\mathrm{Ar}(\nu_e, e^-)\,^{40}\mathrm{K}$ exciting 1^+ states are found to be close to those obtained by the SDPF-VMU-LS interaction in Ref. [10].

Then, EEdf2S is used to study $B(M1)$ in ^{40}Ar and neutral-current reaction $^{40}\mathrm{Ar}(\nu, \nu')\,^{40}\mathrm{K}$. A considerable quenching for the spin gfactor, $q_s^{\mathrm{IV}} \approx 0.4$ is found to reproduce the experimental $B(M1)$ data [42]. The $B(\mathrm{GT})_0$ in the non-charge-exchange channel and neutral-current reaction cross sections are evaluated and compared with those obtained by the SDPF-VMU-LS interaction and RPA calculations. Cross sections for the shell model with the EEdf2S and RPA, where the quenching factors for g_A are determined to be consistent with the experimental $B(M1)$ data, are found to be close to each other in spite of the difference in the GT distributions.

Cross sections induced by forbidden transitions are obtained by RPA using the SGII interaction. Contributions from forbidden transitions become important at high neutrino energy, $E_\nu > 30$ MeV. The total cross sections are obtained, and their sensitivity to the choice of the quenching factor of g_A is indicated. In the present work, the quenching of spin modes is determined by the $B(M1)$ data available in the range of the excitation energy at $E_x = 7.7$–11 MeV [42]. More experimental data for $B(M1)$ at lower excitation energies is required to determine more precise values for the quenching factors. Further expansion of shell-model configuration space is also an important future issue.

ACKNOWLEDGMENTS

T.S. acknowledges support in part by a Grant-in-Aid for Scientific Research under Grants No. JP19K03855 and No.

JP20K03989 of the JSPS KAKENHI. N.S. acknowledges the "Program for Promoting Researches on the Supercomputer Fugaku" (JPMXP1020200105) and MCRP program, University of Tsukuba (wo22i022). The results in this paper were presented at the Workshop on "Neutrino Interaction Measurements for Supernova Neutrino Detection" at Oak Ridge National Laboratory. We would like to thank the Oak Ridge National Laboratory and the workshop participants for stimulating discussion. The authors would like to thank the International Research Network for Nuclear Astrophysics (IReNA) project for the promotion of the compilation and update of nuclear weak rates and cross sections.

[1] A. Ankowski *et al.*, arXiv:1608.07853.

[2] K. G. Balasi, K. Langanke, and G. Martínez-Pinedo, Prog. Part. Nucl. Phys. **85**, 33 (2015).

[3] A. Rubbia, Nucl. Phys. B **66**, 436 (1998); S. Amerio *et al.*, Nucl. Instrum. Methods A **527**, 329 (2004); C. Anderson, M. Antonello, B. Baller, T. Bolton, C. Bromberg, F. Cavanna *et al.*, Phys. Rev. Lett. **108**, 161802 (2012).

[4] Yu. Efremenko and W. R. Hix, J. Phys.: Conf. Ser. **173**, 012006 (2009); D. Akimov *et al.* (COHERENT Collaboration), Science **357**, 1123 (2017); D. Akimov *et al.*, Phys. Rev. Lett. **126**, 012002 (2021).

[5] K. Abe, Y. Haga, Y. Hayato *et al.*, Astropart. Phys. **81**, 39 (2016); K. Abe *et al.*, Nucl. Instrum. Methods A **1027**, 166248 (2022).

[6] K. Abe *et al.* (Hyper-Kamiokande Collaboration), The Astrophys. J. **916**, 15 (2021); K. Abe, Ke. Abe, H. Aihara *et al.*, arXiv:1805.04163; http://www.hyperk.org/.

[7] R. Acciarri *et al.* (DUNE Collaboration), arXiv:1512.06148; W. Altmannshofer, S. Gori, J. Martin-Albo, A. Sousa, and M. Wallbank, Phys. Rev. D **100**, 115029 (2019).

[8] http://juno.ihep.cas.cn/.

[9] E. Kolbe, K. Langanke, G. Martínez-Pinedo, and P. Vogel, J. Phys. G **29**, 2569 (2003).

[10] T. Suzuki and M. Honma, Phys. Rev. C **87**, 014607 (2013).

[11] J. D. Walecka, in *Muon Physics*, edited by V. H. Highes and C. S. Wu (Academic, New York, 1975), Vol. II; J. S. O'Connell, T. W. Donnelly, and J. D. Walecka, Phys. Rev. C **6**, 719 (1972).

[12] T. Otsuka, T. Suzuki, M. Honma, Y. Utsuno, N. Tsunoda, K. Tsukiyama, and M. Hjorth-Jensen, Phys. Rev. Lett. **104**, 012501 (2010).

[13] T. Otsuka, T. Suzuki, R. Fujimoto, H. Grawe, and Y. Akaishi, Phys. Rev. Lett. **95**, 232502 (2005).

[14] Y. Utsuno, T. Otsuka, T. Mizusaki, and M. Honma, Phys. Rev. C **60**, 054315 (1999).

[15] M. Honma, T. Otsuka, T. Mizusaki, M. Hjorth-Jensen, and B. A. Brown, J. Phys.: Conf. Ser. **20**, 7 (2005); M. Honma, T. Otsuka, B. A. Brown, and T. Mizusaki, Phys. Rev. C **65**, 061301(R) (2002); **69**, 034335 (2004).

[16] M. Bhattacharya, C. D. Goodman, and A. Garcia, Phys. Rev. C **80**, 055501 (2009).

[17] M.-K. Cheoun, E. Ha, and T. Kajino, Phys. Rev. C **83**, 028801 (2011).

[18] N. Van Dessel, N. Jachowicz, and A. Nikolakopoulos, Phys. Rev. C **100**, 055503 (2019); N. Van Dessel, A. Nikolakopoulos, and N. Jachowicz, *ibid.* **101**, 045502 (2020).

[19] N. Tsunoda, K. Takayanagi, M. Hjorth-Jensen, and T. Otsuka, Phys. Rev. C **89**, 024313 (2014).

[20] N. Tsunoda, T. Otsuka, N. Shimizu, M. Hjorth-Jensen, K. Takayanagi, and T. Suzuki, Phys. Rev. C **95**, 021304(R) (2017).

[21] D. R. Entem and R. Machleidt, Phys. Rev. C **68**, 041001(R) (2003).

[22] S. Bogner, T. T. S. Kuo, L. Coraggio, A. Covello, and N. Itaco, Phys. Rev. C **65**, 051301(R) (2002).

[23] A. Nogga, S. K. Bogner, and A. Schwenk, Phys. Rev. C **70**, 061002(R) (2004).

[24] T. T. S. Kuo, S. Y. Lee, and K. F. Ratcliff, Nucl. Phys. A **176**, 65 (1971).

[25] E. M. Krenciglowa and T. T. S. Kuo, Nucl. Phys. A **235**, 171 (1974).

[26] T. T. S. Kuo and E. Osnes, *Folded-Diagram Theory of the Effective Interaction in Nuclei, Atoms and Molecules*, Lecture Notes in Physics Vol. 364 (Springer, Berlin, 1990).

[27] M. Hjorth-Jensen, T. T. S. Kuo, and E. Osnes, Phys. Rep. **261**, 125 (1995).

[28] E. M. Krenciglowa and T. T. S. Kuo, Nucl. Phys. A **342**, 454 (1980).

[29] K. Suzuki and S. Y. Lee, Prog. Theor. Phys. **64**, 2091 (1980).

[30] T. T. S. Kuo, F. Krmpotic, K. Suzuki, and R. Okamoto, Nucl. Phys. A **582**, 205 (1995).

[31] Y. Utsuno, T. Otsuka, B. A. Brown, M. Honma, T. Mizusaki, and N. Shimizu, Phys. Rev. C **86**, 051301(R) (2012).

[32] C. Yuan, T. Suzuki, T. Otsuka, F. Xu, and N. Tsunoda, Phys. Rev. C **85**, 064324 (2012).

[33] C. Yuan, M. Liu, N. Shimizu, Zs. Podolyak, T. Suzuki, T. Otsuka, and Z. Liu, Phys. Rev. C **106**, 044314 (2022).

[34] K. Takayanagi, Nucl. Phys. A **852**, 61 (2011); **864**, 91 (2011).

[35] J. Fujita and H. Miyazawa, Prog. Theor. Phys. **17**, 360 (1957).

[36] T. Otsuka, A. Gade, O. Sorlin, T. Suzuki, and Y. Utsuno, Rev. Mod. Phys. **92**, 015002 (2020).

[37] N. Tsunoda, T. Otsuka, K. Takayanagi, N. Shimizu, T. Suzuki, Y. Utsuno, S. Yoshida, and H. Ueno, Nature (London) **587**, 66 (2020).

[38] D. Gazit, S. Quaglioni, and P. Navratil, Phys. Rev. Lett. **103**, 102502 (2009); **122**, 029901 (2019).

[39] M. Kohno, Phys. Rev. C **88**, 064005 (2013); **96**, 059903 (2017).

[40] N. Shimizu, T. Mizusaki, Y. Utsuno, and Y. Tsunoda, Comput. Phys. Commun. **244**, 372 (2019).

[41] D. H. Gloeckner and R. D. Lawson, Phys. Lett. B **53**, 313 (1974).

[42] T. C. Li, N. Pietralla, A. P. Tonchev, M. W. Ahmed, T. Ahn, C. Angell *et al.*, Phys. Rev. C **73**, 054306 (2006).

[43] I. S. Townwer, Phys. Rep. **155**, 263 (1987).

[44] A. Arima, K. Shimizu, W. Bentz, and H. Hyuga, in *Advances in Nuclear Physics*, edited by J. W. Negele and E. W. Vogt (Springer, New York, 1988), Vol. 18.

[45] T. Suzuki, H. Sagawa, and Nguyen van Giai, Nucl. Phys. A **599**, 153 (1996); T. Suzuki, H. Sagawa, and G. Colo, Phys. Rev. C **54**, 2954 (1996).

[46] N. V. Giai and H. Sagawa, Phys. Lett. B **106**, 379 (1981).

[47] T. Suzuki, S. Chiba, T. Yoshida, K. Takahashi, and H. Umeda, Phys. Rev. C **98**, 034613 (2018).

[48] T. Suzuki, Nucl. Phys. A **687**, 119 (2001).

[49] I. Gil-Botella and A. Rubbia, J. Cosmol. Astropart. Phys. **2003**, 009 (2003).